Article

Fragmented Ultrathin Carbon Buffed Copper Clusters for Selective Hydrogenation of *N*-Heteroarenes under Ambient Pressure

Yu Shu, Xiaomei Zhou, Jingnan Yang, Fujun Lan, Wenjiang Li, Zilu Zhang, Wei Li, Qingxin Guan,* and Shengqian Ma*

Read Online

ACCESS | Metrics & More | Article Recommendations | Supporting Information

ABSTRACT: Selective hydrogenation of quinolines to 1,2,3,4-tetrahydroquinolines (py-THQ) realized by cost-effective catalysts holds great importance in the pharmaceutical and agrochemical industries but is challenging due to the high requirement of antipoisoning ability and selectivity. Herein, we propose a universal strategy for the preparation of ultrathin carbon-coated Cu nanoclusters inside the channels of MCM-41 by etching the carbonized template with oxygen-containing gas. The optimized catalyst (Cu/C@MCM-A) exhibits 100% quinoline conversion and 100% py-THQ selectivity at 80 °C and atmospheric pressure. This catalyst also maintained a nearly 100% py-THQ yield at 0.3 MPa for 100 h. In situ characterizations reveal that adjusting the oxygen content in the etching gas enables precise control of the carbon layer thickness and Cu particle size. Experimental results and DFT calculations confirm that the introduction of fragmented ultrathin carbon generates numerous Cu−C interfaces, which can prevent catalyst deactivation by poisoning and reduce the H_2 dissociation barrier by increasing local charge density. The synergy between Cu^0 and Cu^+ species ensures efficient and specific transformation. Moreover, Cu/C@MCM-A demonstrates highly selective hydrogenation activities toward other quinoline derivatives, as well as indole, naphthalene, and indene. This work unlocks a unique route for constructing carbon-confined metal clusters to achieve continuous production in selective hydrogenation.
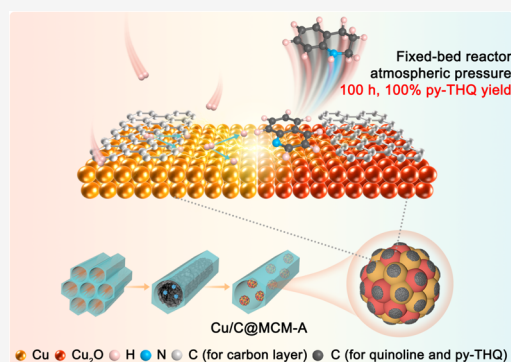
INTRODUCTION

1,2,3,4-Tetrahydroquinoline (py-THQ) skeletons are prevalent and important structural motifs in various bioactive substances and natural alkaloids, as well as drug molecules (e.g., virantmycin and aspoquinolones) with antiviral, antifungal, and anticancer activity properties.[1,2] At present, selective hydrogenation of quinolines is considered a promising approach to produce corresponding compounds due to the great atom economy and simplicity. However, apart from selectivity issues, this direct transformation also involves other challenges such as high reaction energy barriers and potential poisoning by either substrates or their reduced products.[3] Most heterogeneous catalysts in this area with superior performance are noble-metal-based catalysts, (e.g., Pt, Pd, Ru, Rh, Ir, and Au),[4−10] but their insufficient selectivity, poor tolerance for functional groups, and high price restrict their practical applications.[11] Hence, the development of cheap and earth-abundant non-noble-metal catalysts to achieve efficient conversion of quinolines under moderate conditions is critical for the future of the pharmaceutical, polymer, and agrochemical industries.

Recently, supported transition-metal-based catalysts (e.g., Fe, Co, Ni, and Cu)[3,12−16] have attracted extensive attention due to their remarkable capacity in quinoline hydrogenation.

Among them, Cu-based catalysts with more suitable d-band energy and insensitivity to carbon−carbon bonds,[17,18] exhibit unique selectivity advantages (>99%).[19] It has been reported that Cu^+ species could induce the polarization of C═N bond, while Cu^0 species undergo H_2 dissociation and activation.[20] The synergy between these two species is favorable to improving the activity of Cu-based catalysts.[14] Diverse carbon materials are used as electronic buffers to stabilize the Cu^+ sites, and thus a highly active Cu−C interface is established,[21−23] In addition, the core−shell structure of Cu nanoparticles embedded in porous carbon was proved to enhance catalysts' durability against quinoline compared with the fully exposed active sites.[15] Significantly, when the carbon layer coating metal nanoparticles exceeds three, electron passages are hindered, preventing the activation of substrate molecules.[24−26] Cu nanoclusters coated with fragmented ultrathin carbon can generate numerous Cu−C interfaces,

A
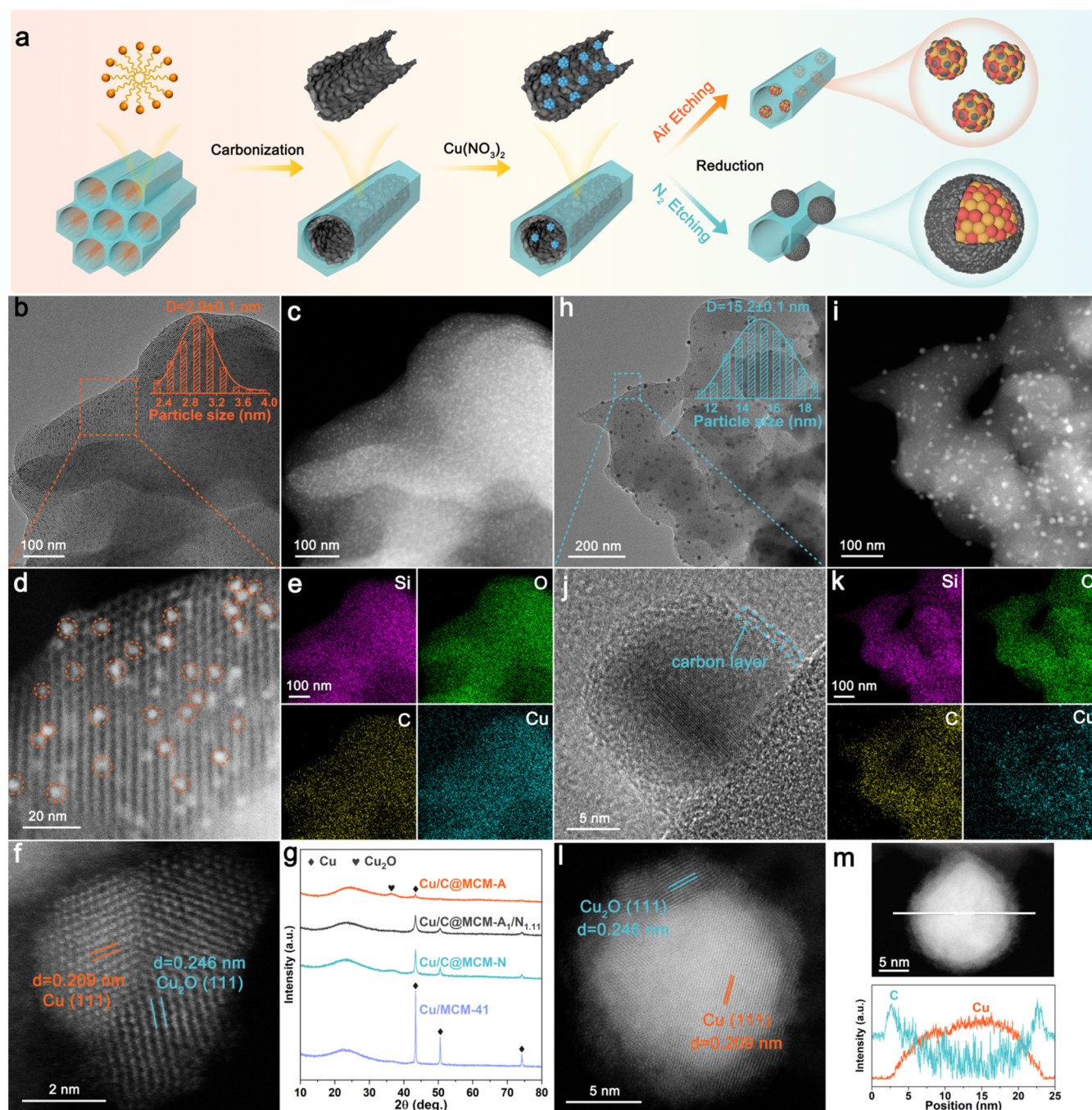
Figure 1. (a) Schematic illustration of the synthesis process in producing Cu/C@MCM-A and Cu/C@MCM-N. (b) TEM image, (c) HAADF-STEM image, (d, f) AC HAADF-STEM image, and (e) EDS mapping of Cu/C@MCM-A. (h) TEM image, (i) HAADF-STEM image, (j) HRTEM image, (k) EDS mapping, (l) AC HAADF-STEM image, and (m) selected Cu nanoparticles and their line EELS profiles in corresponding lines of Cu/C@MCM-N. (g) Wide-angle XRD patterns of Cu/C@MCM-A, Cu/C@MCM-A$_1$/N$_{1.11}$, Cu/C@MCM-N, and Cu/MCM-41.

including the interfaces between Cu atoms and either basal plane or edge carbon atoms. Carbon atoms in the former are in a conjugated network, allowing π electrons to freely transfer throughout the structure and inducing local electron redistribution,[27] and edge carbon atoms in the latter, as the most common intrinsic defects in carbon frameworks, also have certain chemical activity.[28,29] Bao's team found that the smaller the size of graphene, the higher its electrocatalytic activity.[30] Consequently, the catalytic performance of fragmented ultrathin carbon-coated Cu in quinoline selective hydrogenation is worth looking forward to.

Mesoporous silicas are widely recognized for excelling in the confined synthesis of high-loading metal nanoparticles. Deng's group successfully prepared transition metal nanoparticles encapsulated with single-layer graphene inside SBA-15's channels via chemical vapor deposition.[31] And the obtained catalyst displayed impressive performance in the oxygen evolution reaction. Similar works typically require extra carbon sources and high-temperature carbonization in an inert atmosphere to generate stable carbon-coated structures,[32] resulting in a certain waste of resources. Researchers have found that employing Cu foil or O$_2$ as gas-phase additives

enables precise control of the graphene nucleation density.[33,34] O_2 etching allows the chemical activity of its growth edges to be maintained, accelerating its migration and growth.[35]

According to the existing literature, the selective hydrogenation of quinolines is primarily conducted in batch autoclave reactors,[36] which precludes in situ catalyst reduction and causes inevitable exposure to air. Besides, each reaction cycle necessitates many labor-intensive operations. In contrast, the continuous-flow fixed-bed technology can avoid the oxidation of active components and address the recovery issue of supported catalysts. More importantly, fixed-bed systems can break the production restrictions of batch systems and realize the continuous automated production of py-THQ compounds under atmospheric pressure. However, the selective hydrogenation of quinolines in this technology has not been reported.

Herein, we introduced a facile and universal method for the preparation of fragmented ultrathin carbon-coated Cu nanoclusters inside MCM-41's channels, using the template originally present in MCM-41 and assisted with O_2-containing gas for carbonization followed by etching. The optimal catalyst (Cu/C@MCM-A) achieved 100% conversion of quinoline to py-THQ in a continuous-flow fixed-bed reactor at 80 °C and atmospheric pressure, surpassing other catalysts with Cu nanoparticles fully exposed or encapsulated by multiple layers of carbon. Stability tests over 100 h show that Cu/C@MCM-A maintained a nearly 100% py-THQ yield at 0.3 MPa. This catalyst also demonstrated outstanding selective hydrogenation activities toward other quinoline derivatives as well as indole, naphthalene, and indene. In situ characterization revealed the influence of O_2 content in etching gas on the morphology, composition evolution, and spatial distribution of carbon and Cu species, and elucidated the formation mechanism of active sites. Experimental results and DFT calculations confirmed that the Cu−C interface can facilitate H_2 dissociation, while the high content of Cu^+ species ensures the desired selectivity.

■ RESULTS AND DISCUSSION

**Catalyst Preparation and Structural Characterization.** The fabrication route of the Cu/C@MCM-A_x/N$_y$ catalysts is briefly illustrated in Figure 1a. The C@MCM support was achieved by carbonizing the template of CTAB@MCM in air at 300 °C, as reported in our previous work.[37] After $Cu(NO_3)_2 \cdot 3H_2O$ was loaded onto the support via the incipient wetness impregnation method, it was subjected to pyrolysis treatment with gas containing a certain content of O_2, followed by reduction to prepare Cu catalysts. The O_2 content in the pyrolysis atmosphere varied from 0 to 21v/v% by adjusting the proportion of air (A_x) and pure N_2 (N_y). Specifically, the catalysts pyrolyzed under air and N_2 atmosphere were named Cu/C@MCM-A and Cu/C@MCM-N, respectively. If the O_2 content is required to be 10v/v%, the gas flow ratio of air to N_2 should be 1:1.11, and the resulting catalyst was denoted as Cu/C@MCM-A_1/N$_{1.11}$ (detailed preparation procedures are shown in the Supporting Information). The Cu loadings were kept at approximately 10 wt % (Table S1).

Transmission electron microscopy (TEM) and high-angle annular dark-field scanning TEM (HAADF-STEM) images in Figures 1b,c and S3 show that Cu nanoparticles in Cu/C@MCM-A are uniformly distributed in the one-dimensional linear channels, with an average particle size of 2.9 nm, which is further confirmed by numerous ultrafine bright dots

highlighted with colored circles in Figure 1d. Elemental mapping images manifest the homogeneous dispersion of Si, O, C, and Cu throughout the catalyst (Figure 1e). It can be observed that plenty of diminutive Cu particles are still located inside channels of Cu/C@MCM-A_1/N$_{1.11}$, whereas a handful of bulky Cu have migrated to the external surface (Figure S4). As for Cu/C@MCM-N obtained in pure N_2, the vast majority of Cu particles were found on the external surface, with the average size soaring to 15.2 nm (Figures 1h,i and S5). Unsurprisingly, the Cu particle size in Cu/MCM-41 is extremely large, with some exceeding 100 nm (Figure S6). It is worth noting that there is well-marked graphitic carbon surrounding the bulky Cu particles in Cu/C@MCM-N (Figures 1j and S5). Furthermore, the line-scanning electron energy loss spectroscopy (EELS) profile through a Cu nanoparticle also attests that the typical features of the surface species are carbonaceous, with a thickness of at least 1 nm and 3 carbon layers (Figure 1m). According to elemental analysis (EA), the carbon content in Cu/C@MCM-A (3.6 wt %) is far below that in Cu/C@MCM-N (11.0 wt %), which is insufficient to produce a clear carbon layer and extensively encircle one Cu nanoparticle. Beyond that, Figure 1f exhibits a favorable marginal definition of the Cu nanoparticle, suggesting the carbon species in Cu/C@MCM-A tend to be scattered on it in the form of multitudinous microfragments, which are difficult to observe directly. The AC HAADF-STEM images of Cu/C@MCM-A (Figure 1f) and Cu/C@MCM-N (Figures 1l and S5) also provide compelling evidence that Cu species consist of Cu and Cu_2O phases, with lattice distances of 0.209 and 0.246 nm, respectively. These two Cu species, combined with the different carbon coating states, may play a decisive role in hydrogenation activity.

The small-angle X-ray diffraction (XRD) patterns (Figure S1a,b) of all as-prepared and reduced catalysts reveal three distinct peaks at 2.3, 3.8, and 4.4°, linked to the (100), (110), and (200) diffractions of hexagonal symmetry, respectively.[38] Compared with other catalysts, these peaks in Cu/C@MCM-A slightly shift to lower angles, implying a minimum size of the Cu particle. The wide-angle XRD patterns (Figures 1g and S1c,d) of the reduced Cu/C@MCM-A_1/N$_{1.11}$, Cu/C@MCM-N, and Cu/MCM-41 display three sharp and gradually enhanced diffraction peaks at 2θ = 43.4, 50.6, and 74.2°, indexed to the (111), (200), and (220) lattice plane of metallic Cu. Apparently, the characteristic peaks assigned to metallic Cu in Cu/C@MCM-A are fairly faint, suggesting that the air atmosphere during pyrolysis can bring about the tiniest Cu particles and the highest metal dispersion. Besides, a weak peak at 36.5° belonging to the (111) plane of the Cu_2O phase is witnessed, which is consistent with the TEM results. Interestingly, the Cu species of as-prepared carbon-containing catalysts vary with the O_2 content in the pyrolysis gas (Figure S1). When it was 10v/v% and above, the corresponding catalyst precursors exhibited the characteristic diffraction peaks of CuO, similar to Cu/MCM-41−0. Nevertheless, with the O_2 content below 5v/v%, such as Cu/C@MCM-A_1/N$_{3.21}$-0 and Cu/C@MCM-N-0, the peaks pertaining to CuO disappeared, accompanied by the appearance of metallic Cu peaks.

N_2 adsorption−desorption isotherms were determined to recognize the porous structure of Cu/C@MCM-A_x/N$_y$ catalysts (Figure S2 and Table S1). All samples possess type IV isotherms with a small H1 hysteresis loop, signifying an ordered mesoporous structure with a 1D cylindrical channel. Cu/C@MCM-A exhibits the largest specific surface area (S_{BET}
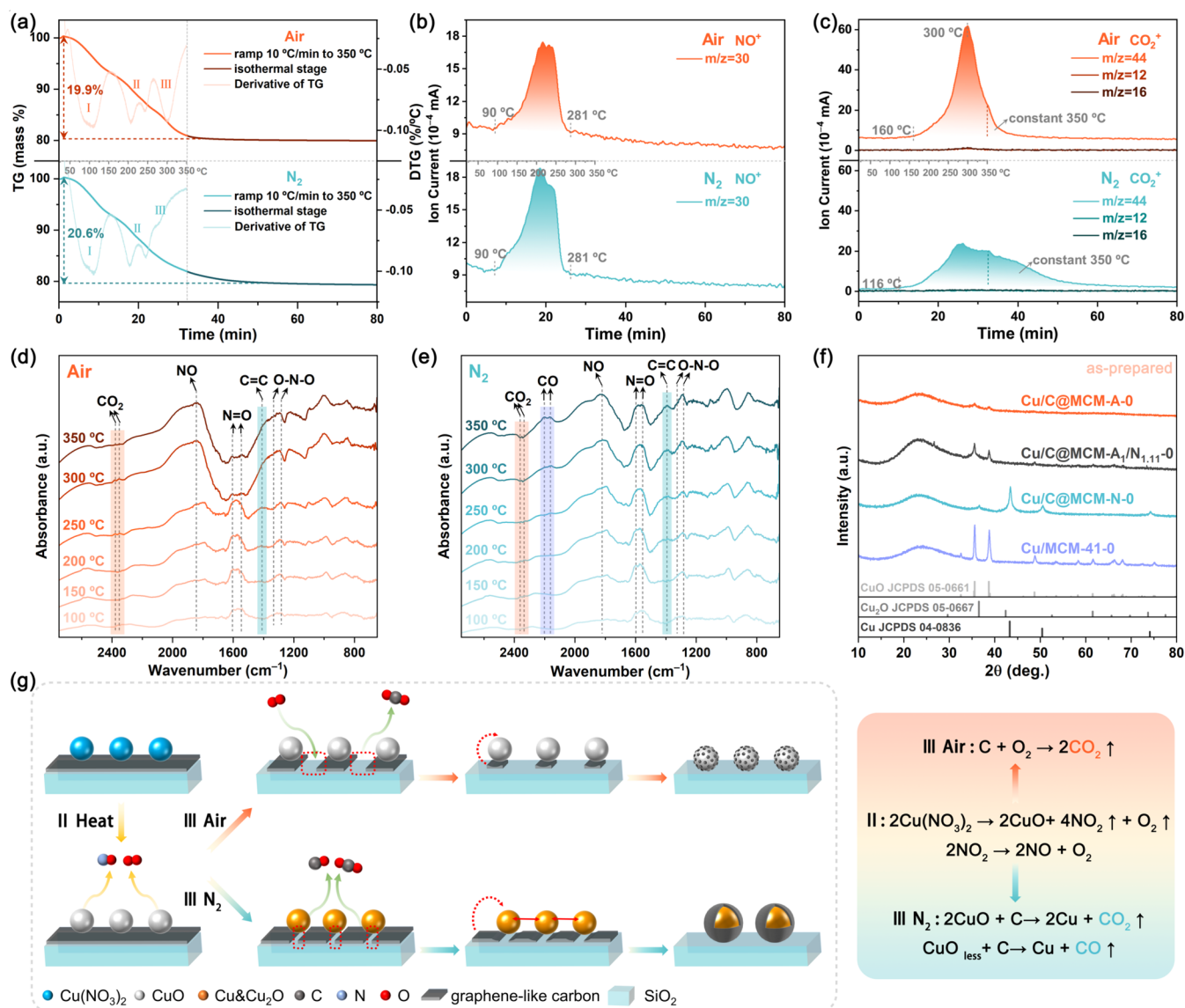
Figure 2. (a) TG and DTG curves, and TG-MS profiles of (b) NO and (c) CO_2 evolution for $Cu(NO_3)_2$/C@MCM in air and nitrogen atmosphere. In situ DRIFTS of C and N species for $Cu(NO_3)_2$/C@MCM in (d) air and (e) nitrogen atmosphere. (f) Wide-angle XRD patterns of as-prepared Cu/C@MCM-A-0, Cu/C@MCM-A_1/$N_{1.11}$-0, Cu/C@MCM-N-0, and Cu/MCM-41-0. (g) Schematic diagram of Cu, C, and N species transformation mechanism for $Cu(NO_3)_2$/C@MCM during the etching process.

= 762 $m^2 \cdot g^{-1}$) and pore volume (V_{total} = 0.82 $cm^3 \cdot g^{-1}$), demonstrating the blockage of Cu particles inside channels is the mildest. Besides, the S_{BET} and V_{total} of the Cu/C@MCM-A_x/N_y catalysts are positively correlated with the O_2 content in the copper salt pyrolysis atmosphere. These results reveal that as the O_2 content tapers off, the amount and the particle size of Cu migrating to the external surface will increase accordingly. Compared with their corresponding supports, Cu/C@MCM-A, Cu/C@MCM-A_1/$N_{1.11}$, Cu/C@MCM-N, and Cu/MCM-41 show the S_{BET} decrease of 16.0, 26.0, 30.1, and 29.7%, respectively. In conclusion, the strategy of adopting C@MCM as the support and air-assisted pyrolysis of copper salt to prepare catalysts is beneficial for encapsulating Cu species and thus restraining particle growth.

To clarify the differences of Cu and carbon species during two pyrolysis atmospheres of air and pure N_2, thermogravimetric-mass spectrometry (TG-MS) was employed. TG test (Figures 2a and S7) of $Cu(NO_3)_2$/C@MCM was conducted

adopting a programmed heating (0−32 min) followed by constant 350 °C for 2 h. The weight loss in air occurs within 36 min (19.9 wt %), while in N_2 it takes place within 52 min (20.6 wt %). The DTG curves verify that there are three main weight loss stages during the heating process in both atmospheres, of which the first two stages are basically similar, but the last one is significantly different. Additionally, MS detected the presence of H_2O (m/z = 18), NO (m/z = 30), and CO_2 (m/z = 44) successively (Figures S7 and 2b,c). The first stage occurs below 160 °C, mainly related to the removal of free water. The second stage is observed between 160 and 275 °C, and meanwhile, NO appears without NO_2, suggesting the decomposition of $Cu(NO_3)_2$. Specifically, $Cu(NO_3)_2$ first underwent pyrolysis into CuO, NO_2, and O_2, and then NO_2 was immediately pyrolyzed into NO and O_2 before being diffused out of channels. The above O_2 also caused the micro etching of carbon inside channels, resulting in the release of a small amount of CO_2. The eventual stage (275−350 °C) was
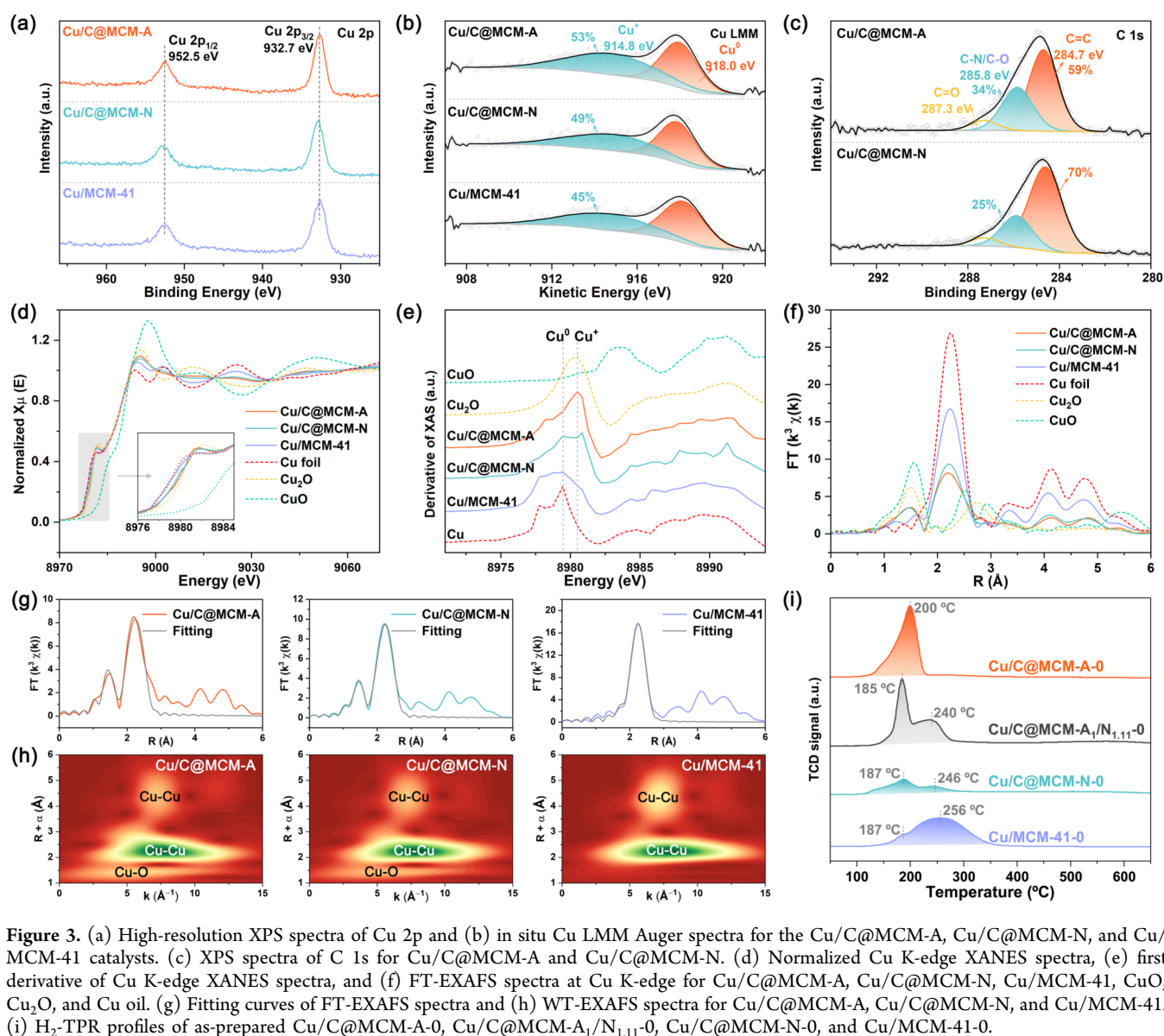
Figure 3. (a) High-resolution XPS spectra of Cu 2p and (b) in situ Cu LMM Auger spectra for the Cu/C@MCM-A, Cu/C@MCM-N, and Cu/MCM-41 catalysts. (c) XPS spectra of C 1s for Cu/C@MCM-A and Cu/C@MCM-N. (d) Normalized Cu K-edge XANES spectra, (e) first derivative of Cu K-edge XANES spectra, and (f) FT-EXAFS spectra at Cu K-edge for Cu/C@MCM-A, Cu/C@MCM-N, Cu/MCM-41, CuO, Cu$_2$O, and Cu oil. (g) Fitting curves of FT-EXAFS spectra and (h) WT-EXAFS spectra for Cu/C@MCM-A, Cu/C@MCM-N, and Cu/MCM-41. (i) H$_2$-TPR profiles of as-prepared Cu/C@MCM-A-0, Cu/C@MCM-A$_1$/N$_{1.11}$-0, Cu/C@MCM-N-0, and Cu/MCM-41-0.

primarily derived from the further oxidation of the residual carbon and its transformation into gaseous carbon oxides. In air, the CO$_2$ peak owns good symmetry at 300 °C and covers the constant 350 °C for only 8 min because the residual carbon was subjected to sufficient etching by O$_2$. However, in N$_2$, it reacts with CuO, as certified by the existence of metallic Cu in Cu/C@MCM-N-0 (Figure 2f).

The possible intermediates generated during the etching process were also investigated by in situ diffused reflectance infrared Fourier transform spectroscopy (in situ DRIFTS) (Figures 2d,e and S8). Regardless of the atmosphere, Cu(NO$_3$)$_2$/C@MCM displays absorbance peaks near 3730 cm^{-1}, ascribed to the O–H stretching vibration of the surface silanol (Si–OH) of MCM-41.[39] Additionally, the N=O stretching vibration peaks (1600−1550 cm^{-1}) and the O−N−O asymmetric stretching vibration (1340−1275 cm^{-1}) are quite prominent even at 100 °C. With the augment of temperature, NO$_3^−$ decomposition happened, and therefore the characteristic peak of gaseous NO emerged (1840 cm^{-1}) from 300 °C.[40] In air, the gaseous CO$_2$ absorbance peaks (2356 and 2334 cm^{-1}) are visible at 300 °C, and

simultaneously, the C=C stretching vibration (1388 cm^{-1}) severely weakens.[41] This result offers definite proof that the carbon inside channels is combusted principally into CO$_2$, whereupon the Cu nanoparticles are clad with carbon fragments. Surprisingly, in N$_2$, except for the weak CO$_2$ absorbance peak observed at 200 °C, the CO characteristic peaks (2200 and 2165 cm^{-1}) and the C=C bond gradually become obvious with the increase of the temperature from 250 to 350 °C.[42] For one thing, it is difficult to distinguish between CO and N$_2$ (same m/z of 28) in the TG-MS tests. For another, based on the fact that the molar amount of carbon (35.68 mmol·g^{-1}) is almost 7 times that of Cu(NO$_3$)$_2$ (5.25 mmol·g^{-1}) in Cu(NO$_3$)$_2$/C@MCM, it is conclusive that a minority of carbon is oxidized by CuO to CO$_2$ and CO, and the majority forms multilayer coated carbon surrounding Cu nanoparticles.

The reduction behavior of the catalysts was explored by H$_2$-TPR (Figure 3i). Considering that Cu species in Cu/C@MCM-N-0 consist of Cu$^+$ and Cu^0 species, this sample was intentionally exposed to air for a period of time so as to amplify and detect microstructure information on all Cu species. Even
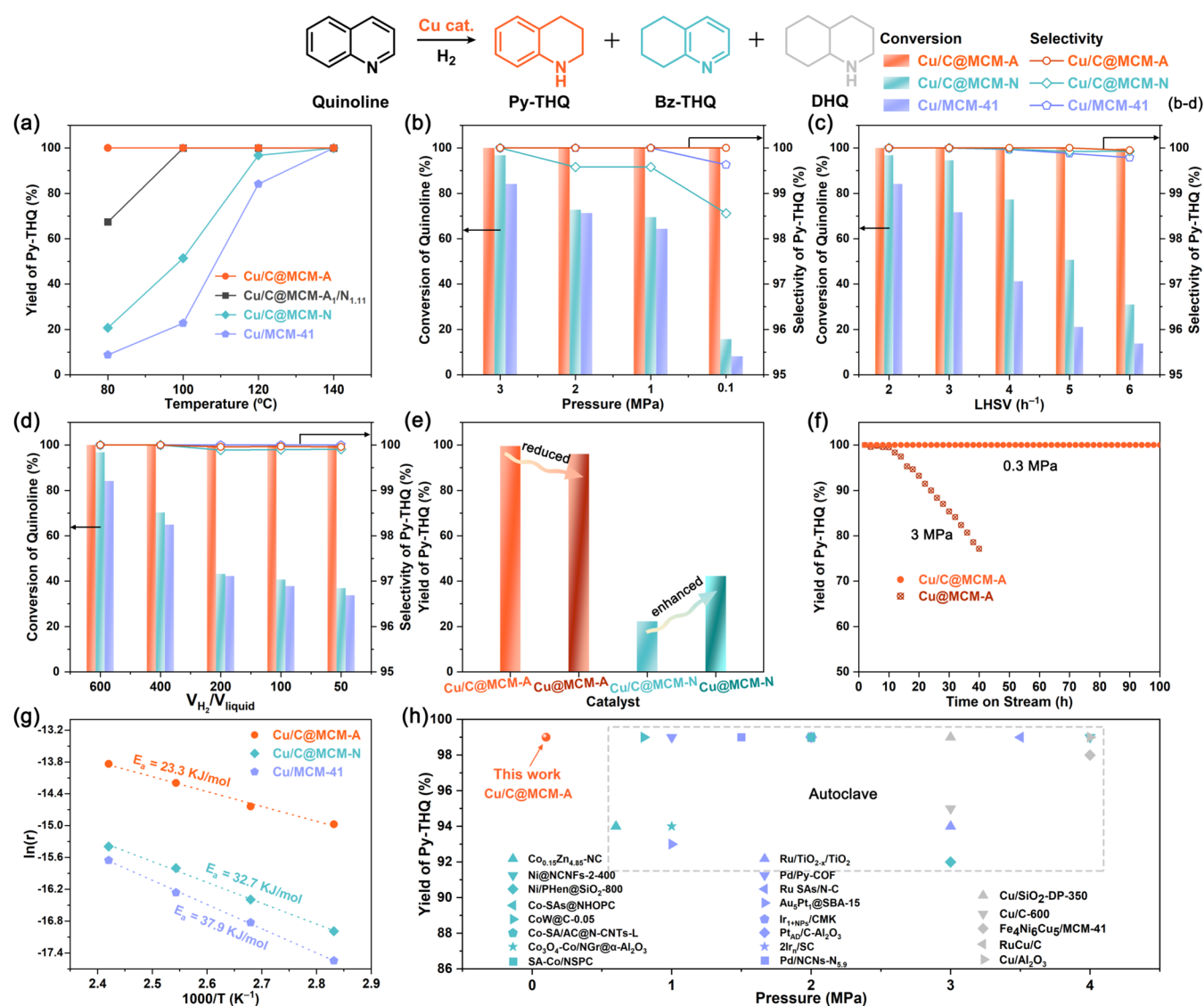
Figure 4. Temperature-dependent (a) py-THQ yield over Cu/C@MCM-A, Cu/C@MCM-A$_1$/N$_{1.11}$, Cu/C@MCM-N and Cu/MCM-41. Quinoline conversion and py-THQ selectivity as functions of (b) H$_2$ pressure, (c) LHSV, (d) V_{H_2}/V_{liquid}, and (g) comparison of apparent activation energy over Cu/C@MCM-A, Cu/C@MCM-N and Cu/MCM-41. (e) Difference of the py-THQ yield over Cu/C@MCM-A, Cu@MCM-A, Cu/C@MCM-N, and Cu@MCM-N. (f) Stability tests on Cu/C@MCM-A and Cu@MCM-A. (h) Performance of Cu/C@MCM-A compared with those of previously reported supported catalysts (Table S4). Reaction conditions: 120 °C (b−f), 3.0 MPa (a, c−e, g), V_{H_2}/V_{liquid} = 600 (a−c, e−g), LHSV = 2 h^{-1} (a, b, d, f), 7 h^{-1} (e).

so, the H$_2$ consumption of Cu/C@MCM-N-0 is apparently less than that of other samples. Cu/C@MCM-A-0 displays the narrowest reduction temperature range from 105 to 230 °C, with only one sharp asymmetric peak centered at 200 °C, indicating that CuO nanoclusters are uniform in size and highly dispersed within the MCM-41's channels. The asymmetry of this peak shape could be attributed to the different distances between the scattered CuO nanoclusters and the orifices. Other samples all show broad double peaks, representing the different distribution states of Cu species. The previous low-temperature peak (187 °C) is also associated with the reduction of CuO encapsulated inside channels. Compared with Cu/C@MCM-A-0, this type of reduction peak shifts toward low temperature by 13 °C, which is triggered by the attenuated interaction between Cu species and support.[43] This phenomenon gives a hint that there is probably more effective electron transfer between CuO nanoclusters and their

surrounding ultrathin carbon fragments than between multi-layer carbon. The latter high-temperature peak is ascribed to the reduction of bulky CuO aggregated on the external surface of MCM-41, following the sequence of Cu/C@MCM-A$_1$/N$_{1.11}$-0 < Cu/C@MCM-N-0 < Cu/MCM-41-0. Combined with TEM results, it can be inferred that the gradual increase in particle size of such Cu species leads to the rise in reduction temperature.[44] In summary, Cu(NO$_3$)$_2$ was originally entirely confined inside the carbon interior modified channels of MCM-41, afterward, the distribution states of Cu species after pyrolysis are profoundly affected by the O$_2$ content in etching atmosphere. Specifically, air can ensure that the spatial location of Cu species remains unchanged. As the O$_2$ content decreases, the tendency for migration and agglomeration would also increase.

In situ X-ray photoelectron spectroscopy (in situ XPS) was implemented to elucidate the chemical compositions and

electronic states of as-prepared and reduced Cu/C@MCM-A, Cu/C@MCM-N, and Cu/MCM-41. The Cu 2p spectra of Cu/C@MCM-A-0 and Cu/MCM-41-0 both exhibit the characteristic peaks of Cu^{2+} species (Figure S9),[17] in agreement with the detection of CuO in XRD tests. As for Cu/C@MCM-N-0, two peaks at 932.7 and 952.5 eV belonging to Cu^+ or/and Cu^0 species are observed. After an in situ reduction treatment, all catalysts display distinct Cu^+ or/and Cu^0 species (Figure 3a). In situ X-ray-induced Auger spectra (in situ XAES) were executed to discriminate these two Cu species (Figure 3b and Table S2). Cu LMM spectra of all reduced catalysts can be deconvoluted into two overlapping peaks around 914.8 and 918.0 eV, ascribed to Cu^+ and Cu^0 species, respectively.[45] Cu^0 is the dominant species in Cu/MCM-41, while Cu^+ increases in other catalysts. Moreover, Cu/C@MCM-A contains slightly more Cu^+ species than Cu/C@MCM-N (53 vs 49%), even though the carbon content is significantly different, which might be induced by the stronger interaction between smaller Cu species and carbon materials in the former. The C 1s spectra manifest that the chemical structures of carbon materials in these two catalysts are constituted by C=C, C−N/C−O, and C=O bonds (Figure 3c).[46] In comparison, the carbon material in Cu/C@MCM-A showed a diminution of the C=C bond and an enhancement of the C−N/C−O bond, confirming its high degree of fragmentation. Given that the difference in N and O species between these two carbon materials is negligible (Figure S10), and their content is fairly low, we predict that the distribution of carbon around Cu nanoparticles may have a certain impact on the catalytic activity.

To probe the local coordination environment, X-ray absorption near-edge structure (XANES) and X-ray absorption fine structure (XAFS) examinations were carried out for the reduced catalysts. The normalized XANES spectra (Figure 3d) show that the Cu K-edge of Cu/MCM-41 is quite similar to that of Cu foil, while the Cu edges of Cu/C@MCM-A and Cu/C@MCM-N lie between those of Cu foil and Cu_2O, demonstrating the valence state of Cu species in the carbon-containing catalysts is between 0 and +1. Notably, the absorption edge of Cu/C@MCM-A shifts slightly toward higher energy compared with Cu/C@MCM-N, due to more electron transfer from Cu atoms to carbon atoms caused by the highly dispersed carbon fragments around Cu nanoclusters. The first derivative of XANES spectra (Figure 3e) exhibits signatures of Cu^0 (8979.4 eV) and Cu^+ (8980.5 eV) species for these two catalysts.[47] In the FT-EXAFS analysis (Figure 3f), all catalysts present a prominent peak (near 2.2 Å) of Cu−Cu scattering consistent with the Cu foil, where Cu/C@MCM-A owns the lowest strength, implying the minimal Cu−Cu coordination number and the tiniest particle size.[48] This speculation can be certified by EXAFS fitting data (Figure 3g and Table S3) and TEM images. In addition, a small peak located at around 1.5 Å also appears in Cu/C@MCM-A and Cu/C@MCM-N, assigned to the Cu−O bond from the Cu_2O phase rather than the CuO phase. As the wavelet transform (WT) spectra depict in Figures 3g and S11, these two carbon-containing catalysts have one more lobe at (k, R) = (5.5, 1.4), attributed to the scattering of Cu−O interaction. The weakening of their second strongest intensity corresponding to the Cu−Cu bond at (k, R) = (7.5, 4.4), compared with Cu/MCM-41, may stem from a significant decrease in the coordination number.[23] Furthermore, Cu/C@MCM-A contains the longest fitted Cu−Cu bond distance of 2.56 Å,

suggesting that the ultrathin carbon fragments give a stronger attraction to Cu species than the large-area-coated multilayer carbons and consequently produce more Cu_2O phase.
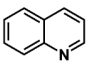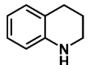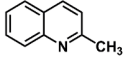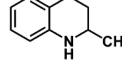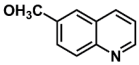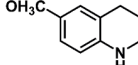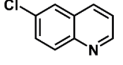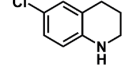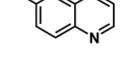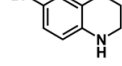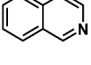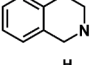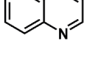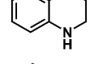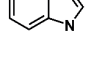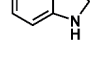
Quinoline Hydrogenation Performances. The catalytic performance of Cu/C@MCM-A_x/N_y catalysts in selective hydrogenation of N-heteroarenes was evaluated in a continuous-flow fixed-bed reactor (Figure S12). As the probe reaction, the quinoline hydrogenation path is presented in Figure 4, where the desired product is partially hydrogenated py-THQ, and byproducts are another partially hydrogenated 5,6,7,8-tetrahydroquinoline (bz-THQ) and fully saturated decahydroquinoline (DHQ). Initially, the dependence of quinoline hydrogenation on reaction temperature was investigated. Py-THQ yield increased with an incremental temperature for all tested catalysts (Figures 4a and S13−S15). Cu/C@MCM-A exhibited remarkable hydrogenation performance, achieving a 100% conversion of quinoline to py-THQ in a quite wide temperature range (70−140 °C), and giving 94% py-THQ yield at 60 °C. In contrast, Cu/C@MCM-A_1/$N_{1.11}$ showed a complete formation of py-THQ above 100 °C, while only 67% yield at 80 °C. Cu/C@MCM-N and Cu/MCM-41 afford crappy hydrogenation activities below 140 °C, with 21% and 9% py-THQ yields at 80 °C, respectively. Apparently, the hydrogenation activity is positively correlated with the oxygen content in the etching gas. Cu/C@MCM-N-0 showed a 68% quinoline conversion at 120 °C, inferior to 97% of Cu/C@MCM-N, hinting that an excessive content of Cu^+ species (68%) is detrimental to the hydrogenation capability. Notably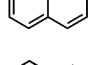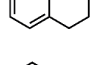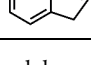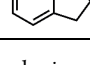, all Cu-based catalysts demonstrated over 99.5% py-THQ selectivity, which is attributed to Cu's inherent insensitivity toward carbon−carbon bonds.

The quinoline hydrogenation over Cu/C@MCM-A under different H_2 pressures, liquid hourly space velocities (LHSV), and H_2-to-liquid ratios (V_{H_2}/V_{liquid}) was also investigated, in comparison with Cu/C@MCM-N and Cu/MCM-41. Cu/C@MCM-A showed extraordinary catalytic activity from atmospheric pressure to 3 MPa (Figure 4b). Unfortunately, Cu/C@MCM-N and Cu/MCM-41 were susceptible to pressure changes, with py-THQ yields of only 15 and 8% at 0.1 MPa, respectively. The preeminent performance of Cu/C@MCM-A at such low H_2 pressure outperforms or rivals previously reported supported catalysts (Figure 4h and Table S4).

Apart from that, the py-THQ yield for Cu/C@MCM-A remained basically 100% within the LHSV range of 2 to 7 h^{-1} (Figures 4c and S16). When the LHSV rose to 9 h^{-1}, quinoline conversion slightly decreased to 97%, which is due to the significantly shortened contact time between the reactant molecules and catalyst at high LHSV. However, quinoline conversion for Cu/C@MCM-N and Cu/MCM-41 dropped to 30 and 13% at the LHSV of 6 h^{-1}. Amazingly, Cu/C@MCM-A also acquitted itself brilliantly in the test of V_{H_2}/V_{liquid} (Figures 4d and S17). As V_{H_2}/V_{liquid} fell from 600 to 10, Cu/C@MCM-A maintained a constant 100% py-THQ yield, whereas it chopped from 96% to 36% for Cu/C@MCM-N, and from 84 to 29% for Cu/MCM-41. Extra evaluation at a fixed atmospheric pressure and recoverability tests further demonstrate the potential of Cu/C@MCM-A for practical industrial applications (Figures S18 and S19).

Aiming at exploring the effect of carbon, further decarbonization treatments were implemented on Cu/C@MCM-A and Cu/C@MCM-N via calcination at 600 °C for 2 h in air, and the obtained catalysts were named Cu@MCM-A and Cu@

Table 1. Hydrogenation of Various Quinoline Derivatives, Indole, Naphthalene, and Indene Catalyzed by the Representative Cu/C@MCM-A Catalyst under Atmospheric Pressure[a]

Entry	Substrate	Product	T (°C)	LHSV (h⁻¹)	Conv. (%)[b]	Sel. (%)[b]
1			120	6	99.5	>99
2			120	4	99.1	>99
3			120	3	99.2	>99
4			120	2	74.8[c]	>99
5			120	0.5	81.7	>99
6			120	1	97.8	>99
7			140	1	93.9	>99
8			140	2	98.5	>99
9			160	1	98.3	>99
10			120	6	99.8	>99

[a]Reaction conditions: 2 wt % substrate in cyclohexane, atmospheric pressure, V_{H_2}/V_{liquid} = 600. [b]Identified by GC and GC−MS. [c]The solvent is changed to methanol due to solubility.

MCM-N, respectively. At the LHSV of 7 h⁻¹, the yield of py-THQ decreased from 100 to 96% over Cu@MCM-A, while it increased from 22 to 42% over Cu@MCM-N, compared with catalysts that have not been decarbonized (Figures 4e and S22). TEM images demonstrate that the Cu particle size in both catalysts was impervious to decarbonization treatment, and thus, the opposite changes in catalytic activity can be ascribed to the different coating states of carbon (Figure S21). We preliminarily speculated that the abundant and rapid exchange of active substances at the junction of carbon fragments and Cu particles is the key to enhancing catalytic activity,[23] instead, the multilayer fully coated carbon is detrimental to their transport. Furthermore, the catalytic stabilities of Cu/C@MCM-A and Cu@MCM-A were assessed (Figures 4f, S20, and S23). Obviously, the performance of Cu@MCM-A was unstable, and the py-THQ yield began to decline after 10 h. On the contrary, the activity of Cu/C@MCM-A remained stable for 100 h at 0.3 MPa and for 54 h at atmospheric pressure with py-THQ yield both approaching 100%. These results provide convincing evidence that carbon fragments are indispensable to outstanding catalytic performances.

The apparent activation energy (Ea) over Cu/C@MCM-A is 23.3 kJ·mol⁻¹ (Figure 4g), lower than that of Cu/C@MCM-N (32.7 kJ·mol⁻¹) and Cu/MCM-41 (37.9 kJ·mol⁻¹). The turnover frequency (TOF) of Cu/C@MCM-A (4.1 h⁻¹) is

over three times higher than that of Cu/C@MCM-N (1.3 h⁻¹) and Cu/MCM-41 (1.1 h⁻¹). Furthermore, the Cu metal surface area (S_{Cu}) over Cu/C@MCM-A is 307.9 m²·g$_{Cu}$⁻¹ (Table S1), which is about 1.5 times that of Cu/C@MCM-N (197.6 m²·g$_{Cu}$⁻¹), and 3 times that of Cu/MCM-41 (98.1 m²·g$_{Cu}$⁻¹). These promising results imply that the abundant active sites with low reaction energy barriers are constituted with a certain amount of oxygen etching treatment. Moreover, the reaction system was extended to the hydrogenation of various quinoline derivatives, indole, naphthalene, and indene under optimized reaction conditions (Tables 1 and S5). The LHSV listed in this table represents the maximum LHSV when the Cu/C@MCM-A catalyst possesses an ideal yield at a fixed reaction temperature. Intriguingly, all of these reactants can be converted smoothly to their corresponding products with selectivity exceeding 99%.

Reaction Mechanisms of Cu/C@MCM-A Catalyst in Quinoline Hydrogenation. To gain deeper insights into how Cu species and their coated fragmented ultrathin carbon contribute to the excellent performance of Cu/C@MCM-A on quinoline hydrogenation, H₂-TPD, in situ DRIFTS, and density functional theory (DFT) calculations were conducted. The capacity for H₂ adsorption of Cu species, carbon fragments, and support is determined by comparing Cu/C@MCM-A, Cu@MCM-A, and MCM-41 via H₂-TPD (Figure S24). All profiles displayed one peak of desorbed H₂ below 300
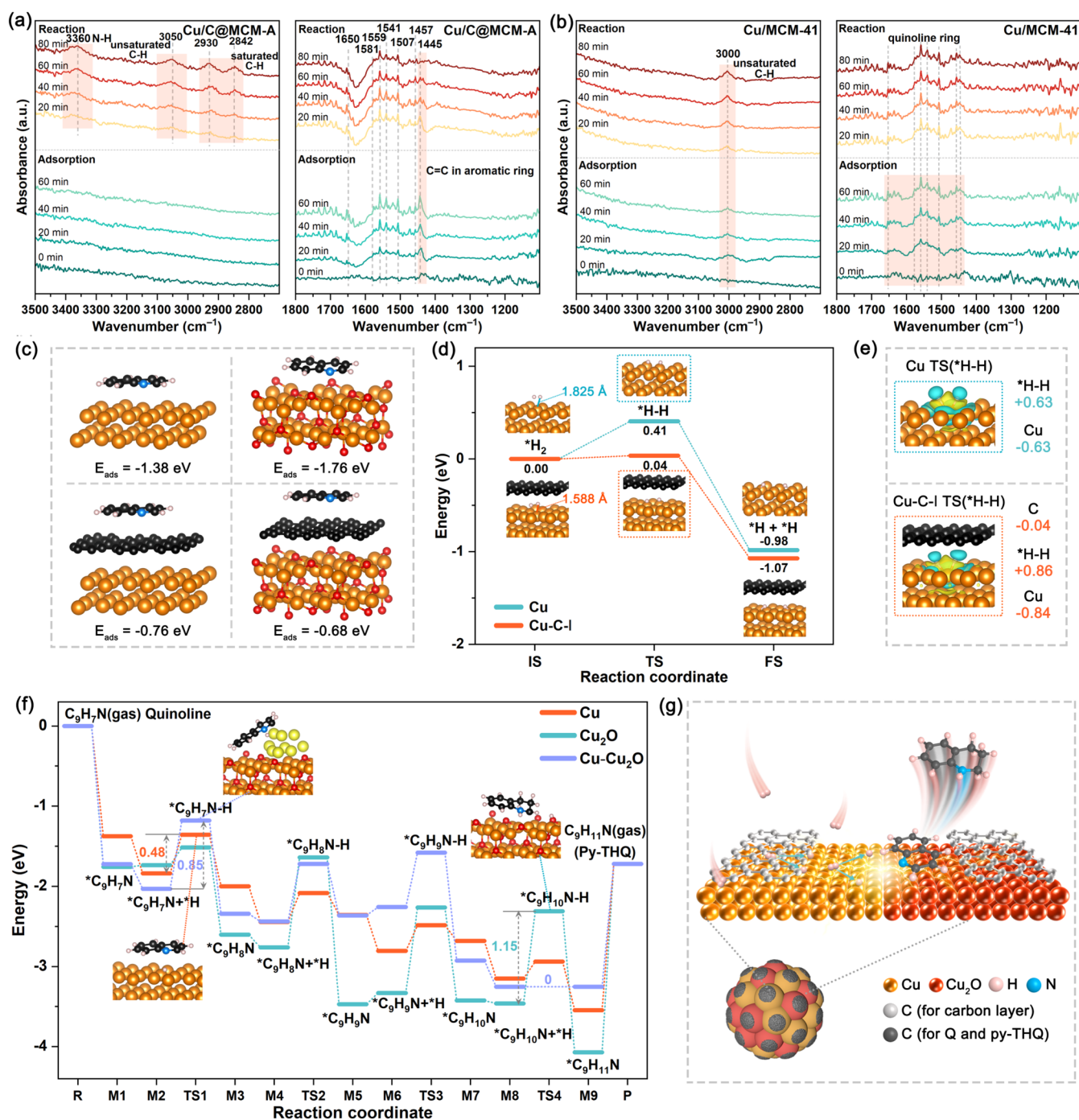
Figure 5. In situ DRIFTS of (a) Cu/C@MCM-A and (b) Cu/MCM-41 after the treatment with quinoline, as well as 10% H$_2$/Ar in sequence at 120 °C and atmospheric pressure. (c) Configurations and energies of quinoline adsorption over Cu, Cu$_2$O, Cu–C–I, and Cu$_2$O–C models. (d) Energy plots of H$_2$ dissociation and (e) differential charge density maps of transition state (*H–H) adsorbed over Cu and Cu–C–I models. (f) Reaction pathways and energies of quinoline selective hydrogenation to py-THQ over Cu, Cu$_2$O, and Cu–Cu$_2$O models. (g) Proposed reaction mechanism for quinoline selective hydrogenation over Cu/C@MCM-A.

°C, which can be ascribed to H$_2$ chemisorbed on Cu active sites and carbon inside channels.[49,50] The peak position and amount of desorbed H$_2$ are both as follows: Cu/C@MCM-A > Cu@MCM-A > MCM-41. Hence, the entire encapsulation of Cu clusters within the channels of MCM-41 ensures the adsorption of a certain amount of H$_2$, and the presence of fragmented ultrathin carbon further promotes H$_2$ enrichment within the channels' microenvironment.

The adsorption and hydrogenation of quinoline on Cu/C@MCM-A and Cu/MCM-41 were recorded by in situ DRIFTS (Figure 5a,b). For quinoline adsorption on both catalysts, the peaks in the 1650−1440 cm^{-1} range assigned to quinoline ring stretching vibrations are observed.[51] Among them, the C═C stretching vibration (1445 cm^{-1}) on Cu/C@MCM-A is stronger than that on Cu/MCM-41, attributed to the substantial adsorption of quinoline by Cu clusters within channels of MCM-41.[52,53] Besides, Cu/MCM-41 displays the

unsaturated C−H stretching vibration near 3000 cm⁻¹, suggesting that some adsorbed quinoline exists on the outer surface of the support, and therefore, all characteristic peaks could be easily detected. The absence of this peak in Cu/C@MCM-A further proves that quinoline is preferentially enriched inside channels, which facilitates the rapid hydrogenation reaction in the microenvironment. After the cessation of quinoline and the introduction of H₂, the spectra on Cu/MCM-41 hardly changed, indicating that the adsorbed quinoline did not react with H₂, which was consistent with the awful performance of this catalyst at 120 °C and atmospheric pressure. In contrast, with the prolonged exposure of Cu/C@MCM-A to H₂, the C=C bond gradually weakened, while the N−H (3360 cm⁻¹), unsaturated C−H (3050 cm⁻¹), and saturated C−H (2930 and 2842 cm⁻¹) stretching vibrations emerged, demonstrating that quinoline underwent transformation to py-THQ inside channels and was subsequently released.

Based on Cu/C@MCM-A's structure characterizations and previous literature,[21−23,54] the combinations of Cu and Cu₂O phases with ultrathin carbon (referred to as Cu−C−I and Cu₂O−C, respectively) were simulated by covering the surface of Cu(111) and Cu₂O(111) with one layer of graphene. The structure of Cu partially (Cu−C−II) covered by carbon was simulated by removing some carbon atoms from the Cu−C−I model. The Cu−Cu₂O interface was simulated by constructing two Cu layers on Cu₂O(111).[55] The optimized models of Cu, Cu−C−I, Cu−C−II, Cu₂O, Cu₂O−C, and Cu−Cu₂O are depicted in Figure S25. The adsorption energies of quinoline on the Cu₂O surface (−1.76 eV) and the Cu−Cu₂O interface (−1.73 eV) are higher than that of Cu surface (−1.38 eV) (Figures 5c and S26), demonstrating that Cu₂O and Cu−Cu₂O are competent to furnish more efficient quinoline adsorption.[14,32] Compared with the bare Cu and Cu₂O, the adsorption energies of quinoline were both reduced on the models of Cu−C−I and Cu₂O−C. Additionally, it has been proved that molecules with C=C bonds tend to be adsorbed on the exposed metal sites more than at the bonding regions between metal atoms and boundary carbon atoms.[56] Therefore, considering the fact that carbon is fragmented surrounding Cu nanoparticles in Cu/C@MCM-A, the exposed Cu sites are more effortless to contact with quinoline molecules than the carbon-covered sites, where the substrate activation is more likely to materialize. Furthermore, it is also speculated that the multilayer carbon (more than three layers) around Cu particles in Cu/C@MCM-N is probably adverse to adsorption and activation of substrates,[24,25] aligning with the performance in Figure 4e.

For hydrogenation reactions in Cu-based catalysts, the dissociation of H₂ typically occurs on Cu metallic sites.[57−59] The energy barrier of H₂ dissociation at the Cu−C−I interface is merely 0.04 eV (Figure 5d), much lower than that at the primordial Cu surface (0.41 eV). And the bond length of Cu−H is shortened from 1.825 Å to 1.588 Å, when single graphene is accommodated on Cu. Moreover, the initial-state H−H bond length stretches from 0.737 to 0.801 Å on the Cu surface, while it stretches to 0.909 Å at the Cu−C−I interface (Figure S28), indicating a better activation of H₂ in the Cu−C−I system. The Cu and Cu−C−I models bound to the important *H intermediate were further investigated through differential charge distribution (Figure 5e). According to Bader charge analysis,[60] for Cu alone, Cu atoms donate 0.63 electrons to *H−H. For Cu−C−I, *H−H get 0.84 and 0.04 electrons from

Cu and C atoms, respectively. These data make it clear that the introduction of monolayer graphene leads to local electron redistribution and increases the local charge density as electrons transfer from Cu and C atoms to H atoms. Since *H−H obtains more free electrons when coupling with Cu−C interface versus Cu alone, the activation energy barrier of H₂ decreases. Notably, H₂ spontaneously dissociates into active H at the Cu−C−II interface, requiring no energy. This originates from the unique local electronic states of the edge C atoms, particularly those located at the zigzag edges,[61] which are filled with massive unpaired π electrons that can effectively accelerate the electron transfer and reduce the related energy barrier.[28,29] Therefore, H₂ dissociation is far more efficient at the interfaces between Cu atoms and either basal plane (Cu−C−I) or edge (Cu−C−II) carbon atoms than on the bare Cu surface. To sum up, the combined advantages of carbon-coated Cu clusters and pore-confined Cu clusters are clearly reflected in the triple confinement of active H, quinoline, and active sites within channels, which is likely to be the reason for Cu/C@MCM-A's splendid performance under atmospheric pressure.

The whole quinoline hydrogenation pathways and the corresponding energy profiles on the Cu and Cu₂O surfaces, and the Cu−Cu₂O interface are displayed in Figures 5f and S29−S31 and Table S6. In view of the different adsorption of H atoms by three sites, an extra intermediate appeared in each step of the H atom attacking and bonding with the substrate, representing the adsorption of the H atom by the current configuration. The rate-limiting steps for quinoline hydrogenation on Cu surface and Cu−Cu₂O interface are the same, both the attack of the first H atom on the N1 site, with energy barriers of 0.48 and 0.85 eV, respectively (Figure 5f, **TS1**). On Cu₂O surface, however, the rate-limiting step is the attack of the fourth H atom on the C2 site, with an energy barrier of 1.15 eV (Figure 5f, **TS4**). Furthermore, unlike the barriers of these four hydrogenation steps that show a gradual decrease on the Cu surface and Cu−Cu₂O interface, they gradually increase on the Cu₂O surface. Interestingly, the fourth hydrogenation step of quinoline at Cu−Cu₂O interface does not require energy, which is clearly the advantage of this interface.[62] The synergy between Cu⁰ and Cu⁺ species encourages efficient transformation,[55] where the relative content of Cu⁺ species reaches up to 53%, resulting in a low *H coverage. At this point, the adsorption/activation rate of quinoline might be slightly faster than the *H transfer rate, and consequently, each quinoline consumes 4 *H to form py-THQ, instead of 10 *H to form DHQ. This possible reaction pathway accounts for the fact that Cu/C@MCM-A combines remarkable hydrogenation activity with high selectivity, as illustrated in Figure 5g.

Extension of the Air-Assisted Etching Method to Co and Ni Metals. Co/C@MCM-A (Figure S33) and Ni/C@MCM-A (Figure S34) were synthesized via the same preparation method as Cu/C@MCM-A. In the wide-angle XRD patterns, the characteristic diffraction peaks corresponding to metallic Co and Ni in these two catalysts are quite weak, with only the major diffraction peaks at 44.2 and 44.5° indexed to Co (111) and Ni (111) lattice plane.[63] TEM images show that Co and Ni nanoclusters (both about 3 nm) are uniformly distributed inside channels of MCM-41. Elemental mapping images also manifest the homogeneous dispersion of Co/Ni and C throughout catalysts. Therefore, the strategy of adopting C@MCM as the support and air-assisted pyrolysis of metal salts and etching of carbon is indeed applicable for the preparation of high-loading Co and Ni nanocluster catalysts,

which holds promise to perform well in other hydrogenation reactions (Figure S35).

CONCLUSIONS

In summary, we managed to synthesize Cu nanoclusters covered with fragmented ultrathin carbon inside the mesochannels of MCM-41. The assembled catalyst (Cu/C@MCM-A) offered 100% conversion of quinoline to py-THQ under exceptionally mild reaction conditions (80 °C and atmospheric pressure) in a continuous-flow fixed-bed reactor. Importantly, this catalyst exhibits a durable stability test over 100 h with a 100% py-THQ yield at 0.3 MPa, outperforming almost all heterogeneous catalysts that we know. Besides, Cu/C@MCM-A shows remarkable hydrogenation activity and chemoselectivity in the partial hydrogenation of other pyridine-like N-heteroarenes and polycyclic aromatic hydrocarbons. In situ characterization attests that the key to catalyst preparation is the etching treatment of precursor impregnated with Cu salts under an oxygen-containing atmosphere. Within the range of 0−21 v/v%, the lower the O_2 content, the larger the Cu particle size, and the thicker the carbon layer, leading to a much inferior catalytic activity. Performance studies and theoretical calculations indicate that the Cu−C interface in Cu/C@MCM-A reduces the energy barrier for H_2 dissociation. Simultaneously, the ultrathin carbon induces more Cu^+ species, and the synergy between it and Cu^0 balances rates for activation (and transference) of quinoline and H_2, guaranteeing the high selectivity of py-THQ. This work provides valuable insights into the mechanism of formation of active sites in catalysts and opens a unique avenue for the construction of carbon-encapsulated metal clusters in selective hydrogenation.

ASSOCIATED CONTENT

Supporting Information

The Supporting Information is available free of charge at https://pubs.acs.org/doi/10.1021/jacs.5c02289.

> Experimental details, materials and methods, characterization results including XRD, N_2 adsorption−desorption, TEM images, TG-MS, XPS, ICP, H_2-TPD, DFT results, and more catalytic data (PDF)

AUTHOR INFORMATION

Corresponding Authors

Qingxin Guan − *State Key Laboratory of Elemento-Organic Chemistry, State Key Laboratory of Advanced Chemical Power Sources, College of Chemistry, Nankai University, Tianjin 300071, China*; Email: qingxinguan@nankai.edu.cn

Shengqian Ma − *Department of Chemistry, University of North Texas, Denton, Texas 76201, United States;* orcid.org/0000-0002-1897-7069; Email: Shengqian.Ma@unt.edu

Authors

Yu Shu − *State Key Laboratory of Elemento-Organic Chemistry, State Key Laboratory of Advanced Chemical Power Sources, College of Chemistry, Nankai University, Tianjin 300071, China*

Xiaomei Zhou − *State Key Laboratory of Elemento-Organic Chemistry, State Key Laboratory of Advanced Chemical*

Jingnan Yang − *State Key Laboratory of Elemento-Organic Chemistry, State Key Laboratory of Advanced Chemical Power Sources, College of Chemistry, Nankai University, Tianjin 300071, China*

Fujun Lan − *State Key Laboratory of Elemento-Organic Chemistry, State Key Laboratory of Advanced Chemical Power Sources, College of Chemistry, Nankai University, Tianjin 300071, China*

Wenjiang Li − *State Key Laboratory of Elemento-Organic Chemistry, State Key Laboratory of Advanced Chemical Power Sources, College of Chemistry, Nankai University, Tianjin 300071, China*

Zilu Zhang − *State Key Laboratory of Elemento-Organic Chemistry, State Key Laboratory of Advanced Chemical Power Sources, College of Chemistry, Nankai University, Tianjin 300071, China*

Wei Li − *State Key Laboratory of Elemento-Organic Chemistry, State Key Laboratory of Advanced Chemical Power Sources, College of Chemistry, Nankai University, Tianjin 300071, China;* orcid.org/0000-0001-7287-8523

Complete contact information is available at: https://pubs.acs.org/10.1021/jacs.5c02289

Author Contributions

All authors have given approval to the final version of the manuscript.

Notes

The authors declare no competing financial interest.

ACKNOWLEDGMENTS

REFERENCES

(1) Muthukrishnan, I.; Sridharan, V.; Menéndez, J. C. Progress in the Chemistry of Tetrahydroquinolines. *Chem. Rev.* **2019**, *119* (8), 5057−5191.

(2) Sridharan, V.; Suryavanshi, P. A.; Menéndez, J. C. Advances in the chemistry of tetrahydroquinolines. *Chem. Rev.* **2011**, *111* (11), 7157−7259.

(3) Puche, M.; Liu, L.; Concepción, P.; Sorribes, I.; Corma, A. Tuning the Catalytic Performance of Cobalt Nanoparticles by Tungsten Doping for Efficient and Selective Hydrogenation of Quinolines under Mild Conditions. *ACS Catal.* **2021**, *11*, 8197−8210.

(4) Fan, S.; Yao, Z.; Cheng, W.; Zhou, X.; Xu, Y.; Qin, X.; Yao, S.; Liu, X.; Wang, J.; Li, X.; Lin, L. Subsurface Ru-Triggered Hydrogenation Capability of TiO_{2-x} Overlayer for Poison-Resistant Reduction of N-Heteroarenes. *ACS Catal.* **2023**, *13* (1), 757−765.

(5) Wang, X.; Chen, W.; Zhang, L.; Yao, T.; Liu, W.; Lin, Y.; Ju, H.; Dong, J.; Zheng, L.; Yan, W.; Zheng, X.; Li, Z.; Wang, X.; Yang, J.; He, D.; Wang, Y.; Deng, Z.; Wu, Y.; Li, Y. Uncoordinated Amine Groups of Metal-Organic Frameworks to Anchor Single Ru Sites as Chemoselective Catalysts toward the Hydrogenation of Quinoline. *J. Am. Chem. Soc.* **2017**, *139* (28), 9419−9422.

(6) Guo, M.; Li, C.; Yang, Q. Accelerated catalytic activity of Pd NPs supported on amine-rich silica hollow nanospheres for quinoline hydrogenation. *Catal. Sci. Technol.* **2017**, *7* (11), 2221−2227.

(7) Everaert, J.; Leus, K.; Rijckaert, H.; Debruyne, M.; Van Hecke, K.; Morent, R.; De Geyter, N.; Van Speybroeck, V.; Van Der Voort, P.; Stevens, C. V. A recyclable rhodium catalyst anchored onto a bipyridine covalent triazine framework for transfer hydrogenation of N-heteroarenes in water. *Green Chem.* 2023, 25 (8), 3267−3277.

(8) Chen, W.; Yao, Z.; Chen, W.; Shen, Q.; Yuan, D.; Zhang, C.; Zhu, Y.; Liang, H. W.; Wang, Y. G.; Song, W.; Cao, C. Fully Exposed Iridium Clusters Enable Efficient Hydrogenation of N-Heteroarenes. *ACS Catal.* 2023, 13 (18), 12153−12162.

(9) Guo, M.; Jayakumar, S.; Luo, M.; Kong, X.; Li, C.; Li, H.; Chen, J.; Yang, Q. The promotion effect of π-π interactions in Pd NPs catalysed selective hydrogenation. *Nat. Commun.* 2022, 13 (1), No. 1770.

(10) Zhao, J.; Yuan, H.; Yang, G.; Liu, Y.; Qin, X.; Chen, Z.; Weng-Chon, C.; Zhou, L.; Fang, S. AuPt bimetallic nanoalloys supported on SBA-15: A superior catalyst for quinoline selective hydrogenation in water. *Nano Res.* 2022, 15 (3), 1796−1802.

(11) Xu, Z. M.; Hu, Z.; Huang, Y.; Bao, S. J.; Niu, Z.; Lang, J. P.; Al-Enizi, A. M.; Nafady, A.; Ma, S. Introducing Frustrated Lewis Pairs to Metal-Organic Framework for Selective Hydrogenation of N-Hetero-cycles. *J. Am. Chem. Soc.* 2023, 145 (27), 14994−15000.

(12) Gong, W.; Yuan, Q.; Chen, C.; Lv, Y.; Lin, Y.; Liang, C.; Wang, G.; Zhang, H.; Zhao, H. Liberating N-CNTs Confined Highly Dispersed Co-N$_x$ Sites for Selective Hydrogenation of Quinolines. *Adv. Mater.* 2019, 31 (49), No. 1906051.

(13) Naveen, K.; Mahvelati-Shamsabadi, T.; Sharma, P.; Lee, S. H.; Hur, S. H.; Choi, W. M.; Shin, T. J.; Chung, J. S. MOF-derived Co/Zn single-atom catalysts for reversible hydrogenation and dehydro-genation of quinoline hydrogen carrier. *Appl. Catal. B Environ.* 2023, 328, No. 122482.

(14) Ma, X.; Huang, G.; Sun, Z.; Liu, Y. Y.; Wang, Y.; Wang, A. Nanocatalysts Derived from Copper Phyllosilicate for Selective Hydrogenation of Quinoline. *ACS Appl. Nano Mater.* 2023, 6 (16), 14756−14766.

(15) Shi, C.; Xu, R.; He, L.; Li, T.; Liu, S.; Yun, R. Endowing Nanoparticles with High Stability on the Hydrogenation Reaction by the Amino Group-Assisted Strategy. *Inorg. Chem.* 2023, 62 (33), 13400−13404.

(16) Zhang, J.; Zheng, C. Y.; Zhang, M. L.; Qiu, Y. J.; Xu, Q.; Cheong, W. C.; Chen, W. X.; Zheng, L. R.; Gu, L.; Hu, Z. P.; Wang, D. S.; Li, Y. D. Controlling N-doping type in carbon to boost single-atom site Cu catalyzed transfer hydrogenation of quinoline. *Nano Res.* 2020, 13 (11), 3082−3087.

(17) Cui, G.; Meng, X.; Zhang, X.; Wang, W.; Xu, S.; Ye, Y.; Tang, K.; Wang, W.; Zhu, J.; Wei, M.; Evans, D. G.; Duan, X. Low-temperature hydrogenation of dimethyl oxalate to ethylene glycol via ternary synergistic catalysis of Cu and acid−base sites. *Appl. Catal. B Environ.* 2019, 248, 394−404.

(18) Huang, F.; Peng, M.; Chen, Y.; Gao, Z.; Cai, X.; Xie, J.; Xiao, D.; Jin, L.; Wang, G.; Wen, X.; Wang, N.; Zhou, W.; Liu, H.; Ma, D. Insight into the Activity of Atomically Dispersed Cu Catalysts for Semihydrogenation of Acetylene: Impact of Coordination Environ-ments. *ACS Catal.* 2022, 12 (1), 48−57.

(19) Yun, R.; Zhang, B.; Zhan, F.; Du, L.; Wang, Z.; Zheng, B. Cu Nanoclusters Anchored on the Metal Organic Framework for the Hydrolysis of Ammonia Borane and the Reduction of Quinolines. *Inorg. Chem.* 2021, 60 (17), 12906−12911.

(20) Yin, A.; Guo, X.; Dai, W. L.; Fan, K. The nature of active copper species in cu-hms catalyst for hydrogenation of dimethyl oxalate to ethylene glycol: Nw insights on the synergetic effect between Cu^0 and Cu$^+$. *J. Phys. Chem. C* 2009, 113 (25), 11003−11013.

(21) Zhao, B.; Chen, F.; Cheng, C.; Li, L.; Liu, C.; Zhang, B. C$_{60}$-Stabilized Cu$^+$ Sites Boost Electrocatalytic Reduction of CO$_2$ to C$_{2+}$ Products. *Adv. Energy Mater.* 2023, 13 (19), No. 2204346.

(22) Li, Y.; Zhang, H.; Chen, T.; Sun, Y.; Rosei, F.; Yu, M. Dual-Interfacial Electrocatalyst Enriching Surface Bonded H for Energy-Efficient CO$_2$-to-CH$_3$OH Conversion. *Adv. Funct. Mater.* 2024, 34 (14), No. 2312970.

(23) Zheng, J.; Huang, L.; Cui, C. H.; Chen, Z. C.; Liu, X. F.; Duan, X.; Cao, X. Y.; Yang, T. Z.; Zhu, H.; Shi, K.; Du, P.; Ying, S. W.; Zhu, C. F.; Yao, Y. G.; Guo, G. C.; Yuan, Y.; Xie, S. Y.; Zheng, L. S. Ambient-pressure synthesis of ethylene glycol catalyzed by C$_{60}$-buffered Cu/SiO$_2$. *Science* 2022, 376 (6590), 288−292.

(24) Yu, L.; Deng, D.; Bao, X. Chain Mail for Catalysts. *Angew. Chem., Int. Ed.* 2020, 59 (36), 15294−15297.

(25) Deng, J.; Ren, P.; Deng, D.; Bao, X. Enhanced electron penetration through an ultrathin graphene layer for highly efficient catalysis of the hydrogen evolution reaction. *Angew. Chem., Int. Ed.* 2015, 54 (7), 2100−2104.

(26) Deng, J.; Yu, L.; Deng, D.; Chen, X.; Yang, F.; Bao, X. Highly active reduction of oxygen on a FeCo alloy catalyst encapsulated in pod-like carbon nanotubes with fewer walls. *J. Mater. Chem. A* 2013, 1 (47), 14868−14873.

(27) Liu, Z.; Liu, Q.; Huang, Y.; Ma, Y.; Yin, S.; Zhang, X.; Sun, W.; Chen, Y. Organic photovoltaic devices based on a novel acceptor material: Graphene. *Adv. Mater.* 2008, 20 (20), 3924−3930.

(28) Jiang, D.-e.; Sumpter, B. G.; Dai, S. Unique chemical reactivity of a graphene nanoribbon's zigzag edge. *J. Chem. Phys.* 2007, 126 (13), No. 134701.

(29) Jiang, Y.; Yang, L.; Sun, T.; Zhao, J.; Lyu, Z.; Zhuo, O.; Wang, X.; Wu, Q.; Ma, J.; Hu, Z. Significant Contribution of Intrinsic Carbon Defects to Oxygen Reduction Activity. *ACS Catal.* 2015, 5 (11), 6707−6712.

(30) Deng, D.; Yu, L.; Pan, X.; Wang, S.; Chen, X.; Hu, P.; Sun, L.; Bao, X. Size effect of graphene on electrocatalytic activation of oxygen. *Chem. Commun.* 2011, 47 (36), 10016−10018.

(31) Cui, X.; Ren, P.; Deng, D.; Deng, J.; Bao, X. Single layer graphene encapsulating non-precious metals as high-performance electrocatalysts for water oxidation. *Energy Environ. Sci.* 2016, 9 (1), 123−129.

(32) Wu, J.; Li, X.; Fu, K.; Cao, D.; Cheng, D. Constructing fully exposed Pt atomically dispersed catalysts for enhanced multifunc-tional selective hydrogenation reactions. *Chem. Eng. J.* 2024, 481, No. 148706.

(33) Chen, J.; Wen, Y.; Guo, Y.; Wu, B.; Huang, L.; Xue, Y.; Geng, D.; Wang, D.; Yu, G.; Liu, Y. Oxygen-aided synthesis of polycrystal-line graphene on silicon dioxide substrates. *J. Am. Chem. Soc.* 2011, 133 (44), 17548−17551.

(34) Kim, H.; Song, I.; Park, C.; Son, M.; Hong, M.; Kim, Y.; Kim, J. S.; Shin, H. J.; Baik, J.; Choi, H. C. Copper-vapor-assisted chemical vapor deposition for high-quality and metal-free single-layer graphene on amorphous SiO$_2$ substrate. *ACS Nano* 2013, 7 (8), 6575−6582.

(35) Zhang, Y.; Sui, Y.; Chen, Z.; Kang, H.; Li, J.; Wang, S.; Zhao, S.; Yu, G.; Peng, S.; Jin, Z.; Liu, X. Role of hydrogen and oxygen in the study of substrate surface impurities and defects in the chemical vapor deposition of graphene. *Carbon* 2021, 185, 82−95.

(36) Wei, Z.; Shao, F.; Wang, J. Recent advances in heterogeneous catalytic hydrogenation and dehydrogenation of N-heterocycles. *Chin. J. Catal.* 2019, 40 (7), 980−1002.

(37) Shu, Y.; Song, X.; Lan, F.; Zhao, C.; Guan, Q.; Li, W. N-Doped Carbon Interior-Modified Mesoporous Silica-Confined Nickel Nano-clusters for Stereoselective Hydrogenation. *ACS Catal.* 2022, 12 (24), 15386−15399.

(38) Song, X.; Guan, Q.; Shu, Y.; Zhang, X.; Li, W. Facile in situ Encapsulation of Highly Dispersed Ni@MCM-41 for the Trans-Decalin Production from Hydrogenation of Naphthalene at Low Temperature. *ChemCatChem.* 2019, 11 (4), 1286−1294.

(39) Aziz, M. A. A.; Jalil, A. A.; Triwahyono, S.; Mukti, R. R.; Taufiq-Yap, Y. H.; Sazegar, M. R. Highly active Ni-promoted mesostructured silica nanoparticles for CO$_2$ methanation. *Appl. Catal. B Environ.* 2014, 147, 359−368.

(40) Wen, X.; Xu, L.; Chen, M.; Shi, Y.; Lv, C.; Cui, Y.; Wu, X.; Cheng, G.; Wu, C.-E.; Miao, Z.; Wang, F.; Hu, X. Exploring the influence of nickel precursors on constructing efficient Ni-based CO$_2$ methanation catalysts assisted with in-situ technologies. *Appl. Catal. B Environ.* 2021, 297, No. 120486.

L

(41) Xu, S.; Chansai, S.; Xu, S.; Stere, C. E.; Jiao, Y.; Yang, S.; Hardacre, C.; Fan, X. CO Poisoning of Ru Catalysts in CO_2 Hydrogenation under Thermal and Plasma Conditions: A Combined Kinetic and Diffuse Reflectance Infrared Fourier Transform Spectroscopy-Mass Spectrometry Study. *ACS Catal.* **2020**, *10* (21), 12828−12840.

(42) Oh, R.; Huang, X.; Hayward, J.; Zheng, Y.; Chen, M.; Park, G. S.; Hutchings, G.; Kim, S. K. Insights into CeO_2 Particle Size Dependent Selectivity Control for CO_2 Hydrogenation Using Co/CeO_2 Catalysts. *ACS Catal.* **2024**, *14* (2), 897−906.

(43) Zhu, Y.; Zhu, Y.; Ding, G.; Zhu, S.; Zheng, H.; Li, Y. Highly selective synthesis of ethylene glycol and ethanol via hydrogenation of dimethyl oxalate on Cu catalysts: influence of support. *Appl. Catal. A-Gen.* **2013**, *468*, 296−304.

(44) Ye, R.-P.; Lin, L.; Yang, J.-X.; Sun, M.-L.; Li, F.; Li, B.; Yao, Y.-G. A new low-cost and effective method for enhancing the catalytic performance of Cu-SiO_2 catalysts for the synthesis of ethylene glycol via the vapor-phase hydrogenation of dimethyl oxalate by coating the catalysts with dextrin. *J. Catal.* **2017**, *350*, 122−132.

(45) Lan, F.; Zhang, H.; Zhao, C.; Shu, Y.; Guan, Q.; Li, W. Copper Clusters Encapsulated in Carbonaceous Mesoporous Silica Nanospheres for the Valorization of Biomass-Derived Molecules. *ACS Catal.* **2022**, *12* (9), 5711−5725.

(46) Cao, J.; Wang, Y.; Chen, J.; Li, X.; Walsh, F. C.; Ouyang, J. H.; Jia, D.; Zhou, Y. Three-dimensional graphene oxide/polypyrrole composite electrodes fabricated by one-step electrodeposition for high performance supercapacitors. *J. Mater. Chem. A* **2015**, *3* (27), 14445−14457.

(47) Karanwal, N.; Kurniawan, R. G.; Park, J.; Verma, D.; Oh, S.; Kim, S. M.; Kwak, S. K.; Kim, J. One-pot, cascade conversion of cellulose to γ-valerolactone over a multifunctional Ru−Cu/zeolite-Y catalyst in supercritical methanol. *Appl. Catal. B Environ.* **2022**, *314*, No. 121466.

(48) Zhang, H.; Zhou, X.; Liu, L.; Lan, F.; Zhao, T.; Qiu, M.; Guan, Q.; Li, W. Assembling Co clusters via nanosized ZIF-67 sprouted from CoAl-LDH nanoflower for selective hydrogenation. *Appl. Catal. B Environ.* **2023**, *338*, No. 123026.

(49) Loy, A. C. M.; Ng, W. L.; Ma, J.; Uddin, M. H.; Vongsvivut, J.; Tobin, M. J.; Samudrala, S. P.; Bhattacharya, S. Deciphering the role of Cu0 and Cuσ+ in engendering the hydrogen production from glycerol reforming over Cu/CeO_2: The effect of different Cu precursors. *Appl. Catal. B Environ.* **2025**, *365*, No. 124865.

(50) Fan, Y. J.; Wu, S. F. A graphene-supported copper-based catalyst for the hydrogenation of carbon dioxide to form methanol. *J. CO2 Util.* **2016**, *16*, 150−156.

(51) Ferri, D.; Bürgi, T. An in situ attenuated total reflection infrared study of a chiral catalytic solid-liquid interface: Cinchonidine adsorption on Pt. *J. Am. Chem. Soc.* **2001**, *123* (48), 12074−12084.

(52) Ferri, D.; Bürgi, T.; Baiker, A. In situ ATR-IR study of the adsorption of cinchonidine on Pd/Al_2O_3: Differences and similarities with adsorption on Pt/Al_2O_3. *J. Catal.* **2002**, *210* (1), 160−170.

(53) Bonalumi, N.; Vargas, A.; Ferri, D.; Bürgi, T.; Mallat, T.; Baiker, A. Competition at chiral metal surfaces: Fundamental aspects of the inversion of enantioselectivity in hydrogenations on platinum. *J. Am. Chem. Soc.* **2005**, *127* (23), 8467−8477.

(54) Li, Y.; Xu, T.; Huang, Q.; Zhu, L.; Yan, Y.; Peng, P.; Li, F. F. C_{60} Fullerenol to Stabilize and Activate Ru Nanoparticles for Highly Efficient Hydrogen Evolution Reaction in Alkaline Media. *ACS Catal.* **2023**, *13* (11), 7597−7605.

(55) Wang, Q. N.; Duan, R.; Feng, Z.; Zhang, Y.; Luan, P.; Feng, Z.; Wang, J.; Li, C. Understanding the Synergistic Catalysis in Hydrogenation of Carbonyl Groups on Cu-Based Catalysts. *ACS Catal.* **2024**, *14* (3), 1620−1628.

(56) Wei, J.; Xiong, S.; Ma, Y.; Cao, D.; Cheng, D. Constructing Co@C nanoparticles with chainmail-structure for highly efficient hydroformylation of 1-hexene. *Chem. Eng. J.* **2024**, *492*, No. 151963.

(57) Yue, H.; Zhao, Y.; Zhao, S.; Wang, B.; Ma, X.; Gong, J. A copper-phyllosilicate core-sheath nanoreactor for carbon-oxygen hydrogenolysis reactions. *Nat. Commun.* **2013**, *4*, No. 2339.

(58) Cheng, J.; Xie, J.; Xi, Y.; Wu, X.; Zhang, R.; Mao, Z.; Yang, H.; Li, Z.; Li, C. Selective Upcycling of Polyethylene Terephthalate towards High-valued Oxygenated Chemical Methyl p-Methyl Benzoate using a Cu/ZrO_2 Catalyst. *Angew. Chem., Int. Ed.* **2024**, *63* (11), No. e202319896.

(59) Gong, J.; Yue, H.; Zhao, Y.; Zhao, S.; Zhao, L.; Lv, J.; Wang, S.; Ma, X. Synthesis of ethanol via syngas on Cu/SiO_2 catalysts with balanced Cu^0-Cu^+ sites. *J. Am. Chem. Soc.* **2012**, *134* (34), 13922−13925.

(60) Bader, R. F. W. A Quantum Theory of Molecular Structure and Its Applications. *Chem. Rev.* **1991**, *91* (5), 893−928.

(61) Zhu, J.; Mu, S. Defect Engineering in Carbon-Based Electrocatalysts: Insight into Intrinsic Carbon Defects. *Adv. Funct. Mater.* **2020**, *30* (25), No. 2001097.

(62) Chang, X.; Wang, T.; Zhao, Z. J.; Yang, P.; Greeley, J.; Mu, R.; Zhang, G.; Gong, Z.; Luo, Z.; Chen, J.; et al. Tuning Cu/Cu_2O Interfaces for the Reduction of Carbon Dioxide to Methanol in Aqueous Solutions. *Angew. Chem., Int. Ed.* **2018**, *57* (47), 15415−15419.

(63) Zhang, H.; Yang, J.; Zhao, T.; Lan, F.; Luo, Y.; Han, F.; Qiao, X.; Guan, Q.; Qiu, M.; Li, W. In-situ constructing ultrafine NiCo alloy confined in LDH nanoflower for efficient selective hydrogenation of furfural. *Chem. Eng. J.* **2024**, *494*, No. 152881.